Two-component Jets of GRB 160623A as Shocked Jet Cocoon Afterglow

Wei Ju Chen[1], Yuji Urata[1] , Kuiyun Huang[2], Satoko Takahashi[3,4,5] , Glen Petitpas[6], and Keiichi Asada[7]
[1] Institute of Astronomy, National Central University, Chung-Li 32054, Taiwan
[2] Center for General Education, Chung Yuan Christian University, Taoyuan 32023, Taiwan
[3] Joint ALMA Observatory, Alonso de Cordova 3108, Vitacura, Santiago, Chile
[4] NAOJ Chile Observatory, Alonso de Córdova 3788, Oficina 61B, Vitacura, Santiago, Chile
[5] Department of Astronomical Science, School of Physical Sciences, SOKENDAI (The Graduate University for Advanced Studies), Mitaka, Tokyo 181-8588, Japan
[6] Harvard-Smithsonian Center for Astrophysics, 60 Garden Street, Cambridge, MA 02138, USA
[7] Academia Sinica Institute of Astronomy and Astrophysics, Taipei 106, Taiwan
Received 2020 January 15; revised 2020 February 9; accepted 2020 February 15; published 2020 March 2

Abstract

Two components of jets associated with the afterglow of the gamma-ray burst (GRB) 160623A were observed with multifrequency observations including long-term monitoring in a submillimeter range (230 GHz) using the Submillimeter Array. The observed light curves with temporal breaks suggest on the basis of the standard forward-shock synchrotron-radiation model that the X-ray radiation is narrowly collimated with an opening angle $\theta_{n,j} < {\sim}6°$, whereas the radio radiation originated from wider jets (${\sim}27°$). The temporal and spectral evolutions of the radio afterglow agree with those expected from a synchrotron-radiation modeling with typical physical parameters, except for the fact that the observed wide jet opening angle for the radio emission is significantly larger than the theoretical maximum opening angle. By contrast, the opening angle of the X-ray afterglow is consistent with the typical value of GRB jets. Since the theory of the relativistic cocoon afterglow emission is similar to that of a regular afterglow with an opening angle of ${\sim}30°$, the observed radio emission can be interpreted as the shocked jet cocoon emission. This result therefore indicates that the two components of the jets observed in the GRB 160623A afterglow are caused by the jet and the shocked jet cocoon afterglows.

1. Introduction

The gamma-ray burst (GRB) is believed to be a stellar explosion accompanied by relativistic outflows and narrowly collimated jets (e.g., Piran 1999). Since direct imaging of GRB jets is impossible, unlike active galactic nucleus (AGN) jets, the jet opening angles of GRBs have been measured by identifying a temporal break in the light curve in multifrequency afterglow monitoring (Sari et al. 1999). The typical value of GRB jet opening angles is ${\sim}3°.5$ (e.g., Racusin et al. 2009), which is in the same order as that of AGN jets (median of $1°.5$ among 373 samples) measured with high-resolution imaging observations (Pushkarev et al. 2017). For populations of both short and long GRBs, understanding of the jet and its structure is essential. There are several methods to constrain the GRB jet structure. An optical spectroscopic study of an associated supernova component has identified a cocoon structure (Izzo et al. 2019). Another method is to measure the detection ratio of off-axis GRB afterglows without prompt high-energy emissions (i.e., orphan GRB afterglow; e.g., Nakar et al. 2002). However, systematic detection of orphan GRB afterglows has never been made (e.g., Huang et al. 2020). Continuous multifrequency afterglow monitoring is another crucial method to constrain the jet structure. In the case of GRB 030329, double-component jets (narrow and wide jets) were identified with optical and radio monitoring, including submillimeter (Berger et al. 2003). Submillimeter and millimeter afterglow observations have played an essential role in

revealing new insights of the GRB afterglow (e.g., Urata et al. 2014, 2019; Huang et al. 2017). Here, we report the long-term monitoring on the GRB 160623A afterglow using the Submillimeter Array (SMA) in conjunction with multifrequency observations. We characterize the dependence of the afterglow flux on time and frequency as $F(t, \nu) \propto t^\alpha \nu^\beta$, where α is the decay index and β is the spectral energy index. We use the cosmological parameters of $\Omega_M = 0.3$, $\Omega_\Lambda = 0.7$, and $H_0 = 70$ km s^{-1} Mpc^{-1} in this Letter.

2. Observations and Results

2.1. Prompt Emission

The *Fermi* Gamma-ray Burst Monitor (GBM) found a signal triggered by GRB 160623A at 05:00:34.23 UT on 2016 June 23 (Mailyan et al. 2016). The *Fermi* Large Area Telescope (LAT) also detected more than 15 photons above 1 GeV until approximately 2 ks (0.02 days) after the trigger time and determined the center position at (R.A., decl.) = (315.24, $+42°.27$) (J2000) with an error radius of $0°.1$ (Vianello et al. 2016). GRB 160623A also was detected by the CALET Gamma-ray Burst Monitor (CGBM) at 04:59:34.27 on 2016 June 23, which was 1 minute earlier than the *Fermi* GBM trigger time (Yamaoka et al. 2016). Hereafter, we use the trigger time of the CGBM as the burst starting time, T_0. All of the CGBM instruments detected the emission and the light curves exhibiting a bright peak at T_0+40 s. By contrast, two of the *Fermi* instruments (GBM and LAT) missed observing the main peak of the event. *Konus–Wind* was also triggered at 04:59:37.594 and detected the emission up to ${\sim}15$ MeV (Tsvetkova et al. 2017). The time-averaged spectrum for the main burst in the 10 keV–10 MeV range was described
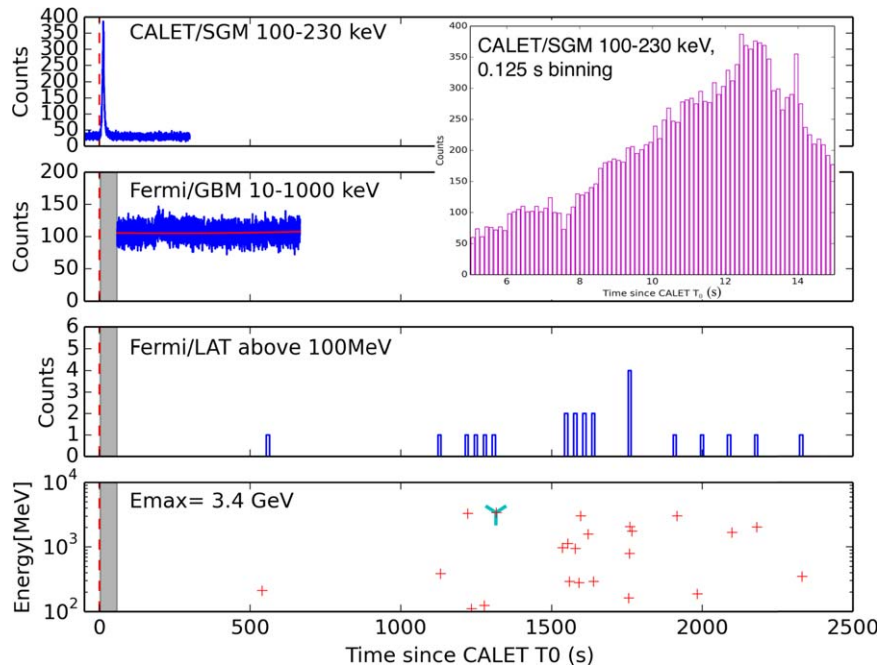
Figure 1. Light curves of (top three panels) counts of GRB 160623A in the prompt phase observed with CALET, *Fermi*/GBM, and *Fermi*/LAT and of (bottom panel) the photon energy distribution observed with *Fermi*/LAT. The gray shaded parts indicate the interval unobserved with *Fermi* due to Earth occultation. The inset shows a zoomed-in time series at around the main peak in the top panel. Variability on a timescale of as short as 0.250 s is visible.

by a Band function with low- and high-energy photon indices of $\alpha = -0.76^{+0.02}_{-0.02}$ of $\beta = -2.80^{+0.05}_{-0.06}$, respectively, and a peak energy $E_p^{\rm obs} = 596^{+15}_{-14}$ keV. The equivalent isotropic radiated energy in the prompt phase at the 10 keV–10 MeV band $E_{\rm iso}$ was estimated as $(2.53 \pm 0.03) \times 10^{53}$ erg (Tsvetkova et al. 2017).

We obtained the light-curve data with 0.125 s time bins observed with CALET from the CGBM Flight Trigger Alert Notices site.[8] We measured 5σ flux variations relative to the neighboring data bins for a timescale of 0.250 s (Figure 1).

The *Fermi*/GBM data were downloaded from the NASA HEASARC *Fermi* GBM Burst catalog. We used the Fermitools version 1.0.7 and HEASOFT for reducing the *Fermi* GBM/LAT data with *gtsrcprob* $p > 0.9$ and a GTI selection of "DATA_QUAL > 0, LAT_CONFIG==1, and ABS(ROCK_ANGLE) < 52." The user contribution code "do_gbm.py" by S. Holland was used for the GBM light-curve analysis. The *Fermi*/LAT photon data were downloaded from the Fermi Science Support Center. Using the likelihood and aperture photometry, we generated the light curve for an energy range of >100 MeV (Figure 1). The highest-energy photon within the 2500 s time coverage was ~3.4 GeV at 1315 s after the burst, which was considerably after the main pulse observed with CALET and *Konus–Wind*. According to the *Fermi*/LAT GRB catalog (Ajello et al. 2019), the energetic photon at 18 GeV was also observed at 12038.53 s after the burst.

Figure 1 shows the light curves obtained by CALET/SGM (100–230 keV), *Fermi*/GBM (10–1000 keV), and *Fermi*/LAT (>100 MeV) along with the photon energy distribution for an energy higher than 100 MeV.

[8] http://cgbm.calet.jp/cgbm_trigger/flight/

2.2. Afterglow

2.2.1. X-Ray and Optical Follow-ups

Neil Gehrels Swift Observatory started follow-up observations at ~40 ks after the burst. The X-Ray Telescope (XRT) identified the X-ray afterglow at R.A. = 21$^{\rm h}$01$^{\rm m}$11$^{\rm s}$22, decl. = +42°13′13″7 with an error radius of 3″5 (Mingo et al. 2016). The X-ray afterglow was observed with XRT until ~12 days after the burst. The Ultraviolet/Optical Telescope (UVOT) also obtained images with the *u* and *v* bands, and no counterparts in the bands were observed (Breeveld & Maselli 2016).

The optical afterglow was detected and its position was determined to be R.A. = 21$^{\rm h}$01$^{\rm m}$11$^{\rm s}$65, decl. = +42°13′15″0 with the Nordic Optical Telescope (NOT; Malesani et al. 2016). The photometric observations of the optical afterglow were executed with Murikabushi (Kuroda et al. 2016), RATIR (Butler et al. 2016), NOT, AZT-33IK (Pozanenko et al. 2016), and Zeiss-1000 (Mazaeva et al. 2016). The redshift was determined to be $z = 0.367$ from the H$_\alpha$, S II, and N II emission lines obtained with the NOT and the Gran Telescope Canarias (Castro-Tirado et al. 2016).

We obtained reduced light curves and spectra in the three periods of 0.47–0.60, 1.3–2.4, and 3.2–11.5 days of the *Swift*/XRT data from the UK Swift Science Data Centre (Evans et al. 2007, 2009). The X-ray light curve is found to be described with a single power-law function with a decay index of $\alpha_X = -1.92 \pm 0.04$ with a reduced $\chi^2/\rm dof = 1.04/86$ (Figure 2). We rebinned the spectra so that each spectral bin contains more than five counts. Using the software XSPEC 12, we perform spectral fitting with a single power law modified with intrinsic and Galactic absorptions, the latter of which is fixed at $N_{\rm H} = 7.17 \times 10^{21}$ cm^{-2} (Pintore et al. 2017). For the first period, we perform spectral fitting, allowing the intrinsic absorption column density to vary. The derived best-fitting values of the intrinsic absorption column
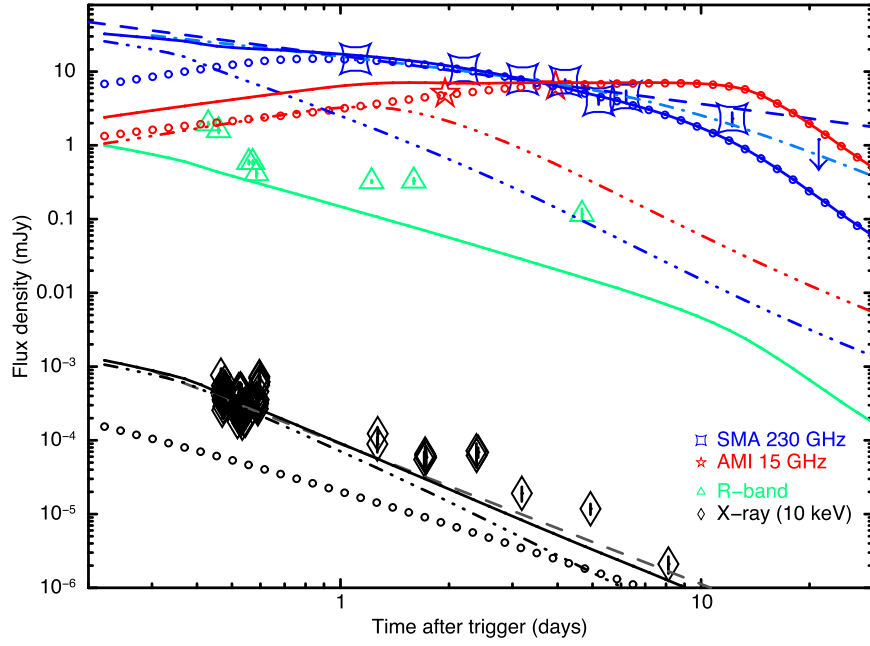
Figure 2. Light curves of the GRB 160623A afterglow in (black) X-rays, (green) optical *R* band, (blue) 230 GHz, and (red) 15 GHz. Blue dashed–dotted line indicates the best-fitting smooth broken power-law function of the 230 GHz light curve. The dashed lines show simple power-law functions with (black) $\alpha_X = -1.92$ and (blue) $\alpha_{230GHz} = -0.65$. The open circle–dotted lines in (black) X-rays, (green) optical, (blue) 230 GHz, and (red) 15 GHz show the best-fitting synchrotron-radiation models for the radio data (i.e., 15 and 230 GHz). The dashed–triple-dot lines in (black) X-rays, (blue) 230 GHz, and (red 15 GHz) show the expected narrow jet component based on the collapsar jet case. The solid lines show the total model function (i.e., summation of the narrow and wide components).
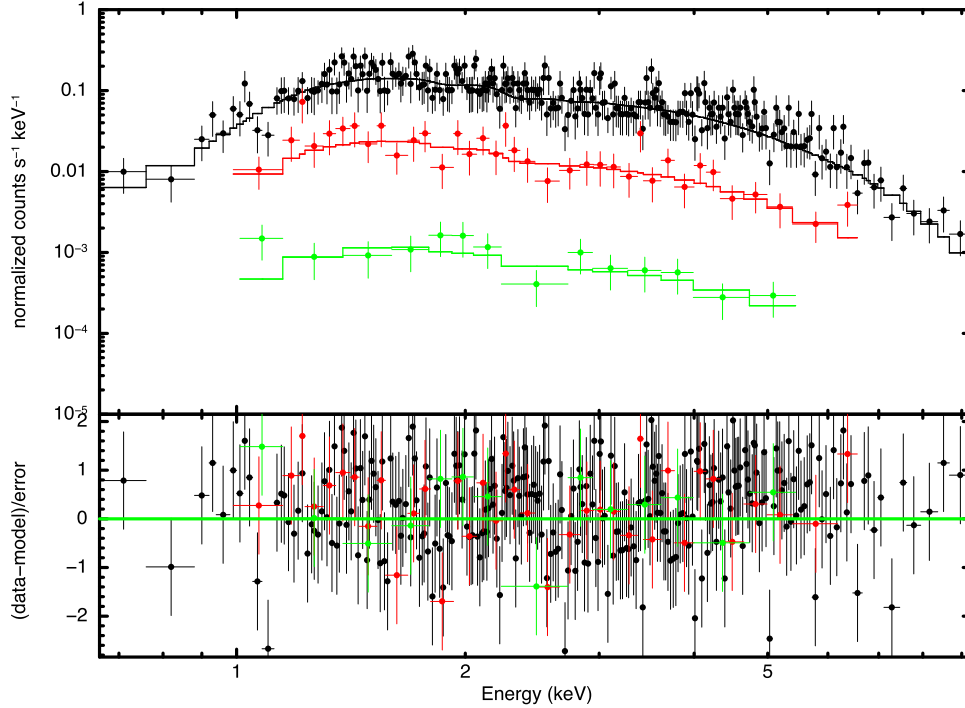
Figure 3. X-ray afterglow spectra in (black) 0.47–0.60 days, (red) 1.3–2.4 days, and (green) 3.2–11.5 along with the best-fitting model with an absorbed power law. Bottom panel shows the residual of the fitting. For the first period (black), we set the intrinsic absorption as a free parameter. The derived best-fitting values of the absorption column density and spectral index were $N_H = (2.7 \pm 0.3) \times 10^{22}$ cm^{-2} and $\beta_X = -0.92 \pm 0.10$, respectively. For the later periods, we fixed the intrinsic absorption obtained with the first period of the spectrum and derived the spectral index to be $\beta_X = -1.0 \pm 0.18$ and $\beta_X = -0.89 \pm 0.33$, respectively.

density and spectral index are $N_H = (2.7 \pm 0.3) \times 10^{22}$ cm^{-2} and $\beta_X = -0.92 \pm 0.10$, respectively, with a reduced $\chi^2/\mathrm{dof} = 0.88/276$ (Figure 3). For the later periods, we fix the intrinsic absorption to the value obtained with the first period of the spectrum. The derived spectral indices are $\beta_X = -1.0 \pm 0.18$ for

the second period with a reduced $\chi^2/\mathrm{dof} = 0.71/35$ and $\beta_X = -0.89 \pm 0.33$ for the third period with a reduced $\chi^2/\mathrm{dof} = 0.63/12$. We therefore find no spectral evolution after 0.47 days, comparing the spectra at the three periods of 0.47–0.60, 1.3–2.4, and 3.2–11.5 days.

Table 1
SMA Observations

Date	t_{start}	t_{end}	N_{antennas}	Time from Trigger (days)	Flux Density (mJy)	Flux Error (mJy)
2016 Jun 24	07:49:04.4	15:19:45.4	5	1.274	14.8	0.5
2016 Jun 25	10:10:03.5	15:58:49.8	7	2.336	10.7	0.4
2016 Jun 26	10:33:10.9	16:02:09.9	7	3.345	7.9	0.4
2016 Jun 27	10:18:05.6	18:05:56.5	7	4.383	7.3	0.5
2016 Jun 28	10:12:26.2	18:00:26.1	7	5.379	4.1	0.5
2016 Jun 29	10:24:08.2	17:45:43.3	7	6.378	4.6	0.9
2016 Jul 5	10:19:21.5	17:14:25.3	7	12.365	2.3	0.5
2016 Jul 14	10:23:49.6	16:42:46.6	8	21.356	1.2	(3σ upper limit)

2.2.2. Submillimeter Array and Radio Follow-ups

We executed submillimeter (230 GHz) follow-up observations using the SMA. The first continuum observation was performed on 2016 June 24, about 1.1 days after the burst. The observation identified a bright ($\sim$15 mJy) submillimeter afterglow, which is one of the brightest GRB afterglows ever detected in the submillimeter range (Urata et al. 2015a). Continuous monitoring was then performed at the same frequency setting on 2016 June 25–29, and July 5 and 14 (Table 1). We reduced the SMA data, using the MIR data-reduction package and Miriad software. The data were flagged and calibrated with the MIR data-reduction package, using the standard procedure, and then images were constructed, using the Miriad software. The total flux was measured with the Common Astronomy Software Applications (McMullin et al. 2007).

We fit the SMA light curve with a simple power-law function. The fitting using the time range from 1.3 to 12.4 days (i.e., all detections) yields a power-law index $\alpha = -0.65 \pm 0.07$ with a reduced $\chi^2/\text{dof} = 4.4/5$. Note that the fitting would be significantly improved if we selected the period before 5 days. The temporal decay is described by the simple power law with $\alpha = -0.54 \pm 0.05$ (reduced $\chi^2/\text{dof} = 1.3/2$). In addition, the extrapolation of the above-mentioned steeper index (i.e., $\alpha = -0.65$) is inconsistent with the upper limit of 21.4 days. Hence, these results indicate that there is a gradual temporal break after $\sim$12 days. We employ a smoothly connected broken power-law function with a smoothness parameter of 1 and fixed decay indices before and after the break of -0.54 and -2, respectively. The fitting yields a temporal break at $t_{R,j} = 27 \pm 14$ days.

The Arcminute Microkelvin Imager (AMI) Large Array detected the radio afterglow at 15 GHz and measured the brightness to be 5.0 ± 0.1 mJy at 2.0 days and 6.3 ± 0.1 mJy at 4.0 days, respectively (Mooley et al. 2016). These measurements indicate that the light curve at 15 GHz exhibited a brightening with $\alpha \sim 0.33$ between 2.0 and 4.0 days. The radio spectral indices between the AMI and SMA bands are also found to be $\beta = \sim 0.27$ at 2 days and $\beta = \sim 0.05$ at 4 days.

3. Discussion

### 3.1. Radiation of Afterglow

The closure relation (e.g., summarized in Zhang & Mészáros 2004) indicates that the X-ray afterglow after 0.46 days was consistent with the relation $\nu_c < \nu_X$ during the post-jet-break phase with the index of the electron energy distribution, $p < 2$ (i.e., $\alpha = (\beta - 3)/2$). The observation with Swift/XRT started some time after the Fermi LAT trigger. Using them, we derive a lower limit of the jet-break time to be $t_{X,j} < 0.46$ days.

Providing that the afterglow emission in the submillimeter originated from the same synchrotron radiation with the X-ray afterglow, the closure relation requires the condition $\nu_{\text{AMI}} < \nu_{\text{SMA}} < \nu a$. Under this condition, the radio afterglow should show decaying with $\alpha = \sim -0.8$ and a steeper spectral index of $\beta = 2$. Although the SMA light curve exhibited decaying, the brightening in the 15 GHz band with the corresponding temporal index of $\alpha = \sim 0.33$ is inconsistent with the relation. The radio spectral indices between the AMI and SMA bands ($\beta = \sim 0.27$ at 2 days and $\beta = \sim 0.05$ at 4 days) are too flat and hence are inconsistent with the expected result. Based on the closure relation, we also consider the two likely conditions $\nu_a < \nu_{\text{AMI}} < \nu_{\text{SMA}} < \nu_m$ and $\nu_{\text{AMI}} < \nu_a < \nu_{\text{SMA}} < \nu_m$ in the $p > 2$ case. The observed results in the AMI (brightening) and SMA (steepness) bands are, however, inconsistent with the temporal evolutions expected in either of the conditions. Therefore, we conclude that the radio emission originated from some different radiation processes or regions from the X-ray emission.

We characterize the SMA and AMI light curves and spectra in the forward-shock synchrotron-radiation framework. Since the optical light curve showed an unusual step decay ($\alpha_{\text{opt}} = \sim -4.6 \pm 0.3$) in the first day, we excluded the optical data in the forward-shock modeling. Employing the boxfit code (van Eerten et al. 2012), which is applicable in the on-axis configuration with a homogeneous circumburst medium (i.e., fixed observing angle as $\theta_{\text{obs}} = 0$), we obtain an optimal model with $\theta_{\text{jet}} = 27°.7$, $E = 7.7 \times 10^{52}$ erg, $n = 70$ cm^{-3}, $p = 2.6$, $\epsilon_B = 2.0 \times 10^{-5}$, and $\epsilon_e = 1.9 \times 10^{-1}$. These values are consistent with those of a typical GRB afterglow (Panaitescu & Kumar 2002; van Eerten et al. 2012; Urata et al. 2015b; Huang et al. 2017), except for a wider jet opening angle in our result than that of a typical GRB afterglow. Note that the relatively higher circumburst density is consistent with a high intrinsic absorption obtained from the X-ray spectrum of GRB 160623A (e.g., Fiore et al. 2007). Figure 4 shows the histogram of GRB jet opening angles. The jet opening angle of the GRB 160623A radio afterglow is the largest among all GRBs. Figure 2 demonstrates that the model functions well describe the observed radio light curves. With the obtained physical parameters, we also derive the expected light curves and confirm that the emission from the wide jet in X-ray and optical bands should be negligible in observations.

3.2. Jet Opening Angle and Cocoon Radiation

We further evaluate the jet opening angles on the basis of Equation (1) of Frail et al. (2001), using the observed isolated equivalent energy and assuming $\eta = 0.2$, where η is the radiative efficiency. The jet opening angle for the radio afterglow is estimated, using the temporal break in 230 GHz,
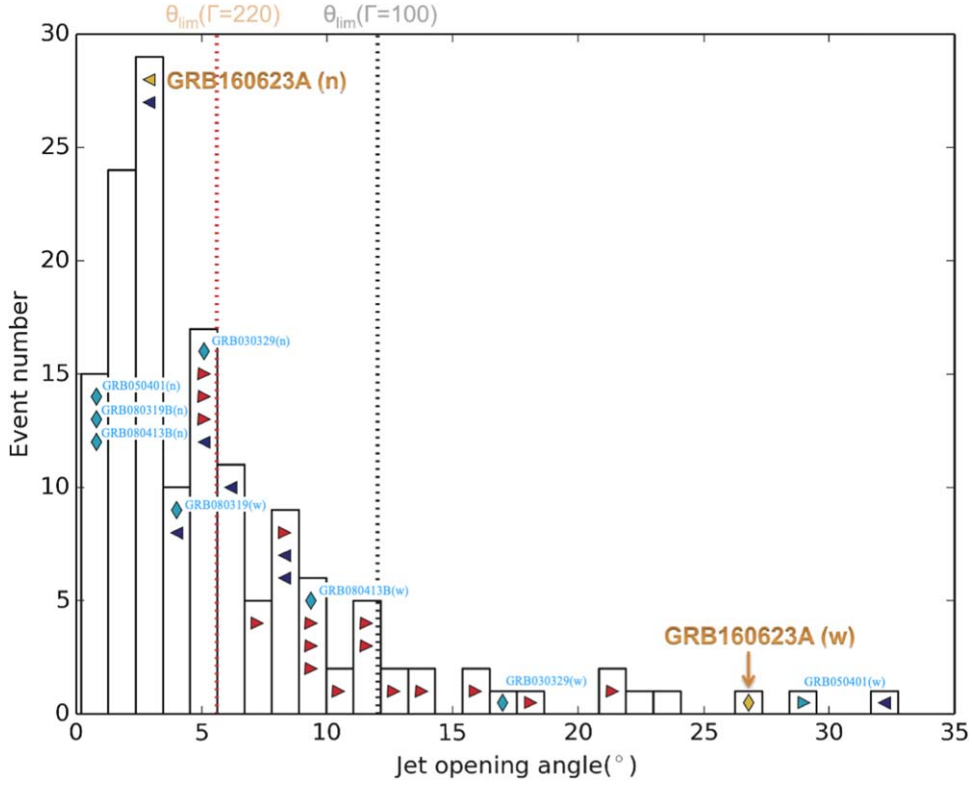
Figure 4. Distribution of the jet opening angles of GRB 160623A and other GRBs. The narrow and wide jets of GRB 160623A are highlighted with yellow marks. Upper and lower limits are indicated by blue and red arrows, respectively. The orange dotted line indicates the maximum jet opening angle for GRB 160623A. The black dotted line indicates the maximum jet opening angle with $\Gamma_0 = 100$. Four events reported as double jets (GRB 030329, GRB 050401, GRB 080319B, and GRB 080413B) are also highlighted with cyan diamond marks. We collected the jet opening angles of other GRBs from the literature (Frail et al. 2001; Berger et al. 2003; Bloom et al. 2003; Ghirlanda et al. 2004; Friedman & Bloom 2005; Racusin et al. 2009; Cenko et al. 2010, 2011; Filgas et al. 2011). The measurement methods of their jet opening angles are described in individual references. Basically, the methods are identical to one another, as described in Sari et al. (1999) and according to afterglow modeling within the framework of the forward-shock synchrotron radiation.

to be $\theta_{R,j} = 13^\circ.0 \pm 2^\circ.8$ for the circumburst density $n = 1$ cm^{-3} and $22^\circ.2 \pm 5^\circ.3$ for $n = 70$ cm^{-3}, where $n = 1$ and $n = 70$ cm^{-3} are for the typical value and for the estimated one from the radio afterglow modeling, respectively. Alternatively, using the explosion energy derived on the basis of the afterglow modeling, we estimate the jet opening angle of GRB 160623A to be $26^\circ.3$. These values are more than twice larger than the typical jet opening angle of the GRB. In the same manner, we also estimate the upper limits of the jet opening angle for the X-ray afterglow to be $\theta_{X,j} < 2^\circ.8$ for $n = 1$ cm^{-3}, $\theta_{X,j} < 4^\circ.7$ for $n = 70$ cm^{-3}, and $\theta_{X,j} < 5^\circ.6$ for $n = 70$ cm^{-3} from the explosion energy. These upper limits are consistent with the typical value of GRB jet opening angles (Figure 4).

The origin of the wide jet emission may require an additional component to those common for regular GRB afterglows. Mizuta & Ioka (2013) constrained the maximum opening angle $\theta_{j,\text{max}}$ to be $1/5\Gamma_0$, where Γ_0 is the initial Lorentz factor (i.e., $\theta_{j,\text{max}} < \sim 12^\circ$ for $\Gamma_0 > 100$). We estimate the initial Lorentz factor of GRB 160623A to be $\Gamma_0 > 220$ from the prompt time variability of 0.250 s (Lithwick & Sari 2001; Golkhou et al. 2015) and, accordingly, the maximum opening angle of this event to be $\theta_{j,\text{max}} < 5^\circ.5$. Consequently, the radio afterglow jet angle of GRB 160623A does not agree with the theoretical maximum opening angle, whereas the upper limit of the X-ray afterglow jet angle does. According to Nakar & Piran (2017), the typical opening angle of the relativistic cocoon afterglow is $\sim 30^\circ$. Since the theory

of the relativistic cocoon afterglow emission is similar to that of the regular afterglow (Nakar & Piran 2017), the parameters estimated above characterize the shocked jet cocoon emission. Assuming the energy ratio of wide to narrow components as $E_{\text{wide}}/E_{\text{narrow}} \sim 0.1$ (i.e., the collapsar jet case; Peng et al. 2005) and the identical microphysical parameters (n, ϵ_B, and ϵ_e) to the wide jet (Nakar & Piran 2017) with a synchrotron slope of $p \sim 2$ (based on the X-ray spectrum) and a narrow jet opening angle of $5^\circ.5$, we confirmed that the expected narrow jet components in X-ray and radio bands can describe the observed light curves (Figure 2). Considering the prompt phase of GRB 160623A missed by *Fermi*/LAT (Figure 1), the huge total energy ($\sim 8.5 \times 10^{53}$ erg) is likely reasonable being the same as other energetic ($> 10^{54}$ erg) *Fermi*/LAT events (e.g., Abdo et al. 2009; Urata et al. 2012; Ajello et al. 2019). In fact, even the late phase radiation in 100 MeV–10 GeV reached $(2.4 \pm 0.3) \times 10^{52}$ erg (Ajello et al. 2019). This result therefore implies that the GRB 160623A radio afterglow originated from a relativistic cocoon afterglow.

The afterglows with double jet components are rarely observed. There are only five events (shown in Figure 4), and one of the notable events is GRB 030329 with $\theta_{n,j} = 5^\circ.2$ and $\theta_{w,j} = 17^\circ.2$ (Berger et al. 2003). Since afterglows of GRB 030329 and GRB 160623A were densely monitored in the millimeter/submillimeter ranges, further millimeter/submillimeter observations would address the wide jet and shocked cocoon radiation.

ORCID iDs

Yuji Urata ● https://orcid.org/0000-0001-7082-6009
Satoko Takahashi ● https://orcid.org/0000-0002-7287-4343

References

Abdo, A. A., Ackermann, M., Ajello, M., et al. 2009, ApJL, 706, L138
Ajello, M., Arimoto, M., Axelsson, M., et al. 2019, ApJ, 878, 52
Berger, E., Kulkarni, S. R., Pooley, G., et al. 2003, Natur, 426, 154
Bloom, J. S., Frail, D. A., & Kulkarni, S. R. 2003, ApJ, 594, 674
Breeveld, A., & Maselli, A. 2016, GCN, 19568, 1
Butler, N., Watson, A. M., Kutyrev, A., et al. 2016, GCN, 19567, 1
Castro-Tirado, A. J., Valeev, A. F., Jeong, S., et al. 2016, GCN, 19710, 1
Cenko, S. B., Frail, D. A., Harrison, F. A., et al. 2010, ApJ, 711, 641
Cenko, S. B., Frail, D. A., Harrison, F. A., et al. 2011, ApJ, 732, 29
Evans, P. A., Beardmore, A. P., Page, K. L., et al. 2007, A&A, 469, 379
Evans, P. A., Beardmore, A. P., Page, K. L., et al. 2009, MNRAS, 397, 1177
Filgas, R., Krühler, T., Greiner, J., et al. 2011, A&A, 526, A113
Fiore, F., Guetta, D., Piranomonte, S., et al. 2007, A&A, 470, 515
Frail, D. A., Kulkarni, S. R., Sari, R., et al. 2001, ApJL, 562, L55
Friedman, A. S., & Bloom, J. S. 2005, ApJ, 627, 1
Ghirlanda, G., Ghisellini, G., & Lazzati, D. 2004, ApJ, 616, 331
Golkhou, V. Z., Butler, N. R., & Littlejohns, O. M. 2015, ApJ, 811, 93
Huang, K., Urata, Y., Takahashi, S., et al. 2017, PASJ, 69, 20
Huang, Y. J., Urata, Y., Huang, K. Y., et al. 2020, ApJ, submitted
Izzo, L., de Ugarte Postigo, A., Maeda, K., et al. 2019, Natur, 565, 324
Kuroda, D., Hanayama, H., Miyaji, T., et al. 2016, GCN, 19572, 1
Lithwick, Y., & Sari, R. 2001, ApJ, 555, 540
Mailyan, B., Toelge, K., & Roberts, O. 2016, GCN, 19555, 1
Malesani, D., de Ugarte Postigo, A., de Pasquale, M., et al. 2016, GCN, 19708, 1
Mazaeva, E., Kusakin, A., Reva, I., et al. 2016, GCN, 19574, 1
McMullin, J. P., Waters, B., Schiebel, D., Young, W., & Golap, K. 2007, in ASP Conf. Ser. 376, Astronomical Data Analysis Software and Systems XVI, ed. R. A. Shaw, F. Hill, & D. J. Bell (San Francisco, CA: ASP), 127
Mingo, B., Beardmore, A. P., D'Ai, A., et al. 2016, GCN, 19558, 1
Mizuta, A., & Ioka, K. 2013, ApJ, 777, 162
Mooley, K. P., Staley, T. D., Fender, R. P., et al. 2016, GCN, 19609, 1
Nakar, E., & Piran, T. 2017, ApJ, 834, 28
Nakar, E., Piran, T., & Granot, J. 2002, ApJ, 579, 699
Panaitescu, A., & Kumar, P. 2002, ApJ, 571, 779
Peng, F., Königl, A., & Granot, J. 2005, ApJ, 626, 966
Pintore, F., Tiengo, A., Mereghetti, S., et al. 2017, MNRAS, 472, 1465
Piran, T. 1999, PhR, 314, 575
Pozanenko, A., Mazaeva, E., Minaev, P., et al. 2016, GCN, 19561, 1
Pushkarev, A. B., Kovalev, Y. Y., Lister, M. L., et al. 2017, MNRAS, 468, 4992
Racusin, J. L., Liang, E. W., Burrows, D. N., et al. 2009, ApJ, 698, 43
Rossi, E. M., Perna, R., & Daigne, F. 2008, MNRAS, 390, 675
Sari, R., Piran, T., & Halpern, J. P. 1999, ApJL, 519, L17
Tsvetkova, A., Frederiks, D., Golenetskii, S., et al. 2017, ApJ, 850, 161
Urata, Y., Huang, K., Asada, K., et al. 2015a, AdAst, 2015, 165030
Urata, Y., Huang, K., & Petitpas, G. 2016, GCN, 19584, 1
Urata, Y., Huang, K., Takahashi, S., et al. 2014, ApJ, 789, 146
Urata, Y., Huang, K., Yamaoka, K., et al. 2012, ApJL, 748, L4
Urata, Y., Huang, K., Yamazaki, R., & Sakamoto, T. 2015b, ApJ, 806, 222
Urata, Y., Toma, K., Huang, K., et al. 2019, ApJL, 884, L58
van Eerten, H., van der Horst, A., & MacFadyen, A. 2012, ApJ, 749, 44
Vianello, G., Dirirsa, F., Omodei, N., et al. 2016, GCN, 19553, 1
Yamaoka, K., Yoshida, A., Sakamoto, T., et al. 2016, GCN, 19597, 1
Zhang, B., & Mészáros, P. 2004, IJMPA, 19, 2385